Applied Water Science (2024) 14:191
https://doi.org/10.1007/s13201-024-02254-8

ORIGINAL ARTICLE

Synthesis and characterization of a bimetal nickel manganese oxysulfide (NiMnOS) catalyst for the reduction of methylene blue dye

Abraham Solomon Kasa[1] · Dinsefa Mensur Andoshe[1] · Noto Susanto Gultom[2] · Dong-Hau Kuo[2] · Xiaoyun Chen[3] · Hairus Abdullah[2,4] · Osman Ahmed Zelekew[1]

Received: 15 July 2022 / Accepted: 28 July 2024 / Published online: 8 August 2024

Abstract

Noble metal-free nickel manganese oxysulfide (NiMnOS) catalysts were successfully prepared via a facile and eco-friendly approach at a low synthesis temperature of 90 °C in a water bath. The catalysts were synthesized by varying Ni: Mn molar ratios such as 25:75, 50:50, 75:25 and abbreviated as NiMnOS-25, NiMnOS-50, and NiMnOS-75, respectively. The bare NiOS and MnOS were also prepared for comparison purposes. The characterizations of the prepared samples were conducted with different techniques, and the catalytic activity was investigated through the reduction of methylene blue (MB) dye in the presence of $NaBH_4$ in an aqueous solution. Among the prepared catalysts, NiMnOS-25 exhibited excellent performance and reduced 98.46% of MB within 5 min. However, NiOS, NiMnOS-50, NiMnOS-75, and MnOS were reduced 9.6%, 98.41%, 97.04%, and 6.40% of MB dye, respectively, within 7 min. The catalytic reduction activity could be mainly attributed to the synergistic effects of the metals (Ni and Mn), more exposed active sites. Therefore, the bimetal NiMnOS catalyst could be a promising candidate for the reduction of organic dyes in wastewater treatment technologies.

Keywords Bimetallic oxysulfide · NiMnOS · Catalyst · Reduction · Methylene blue

Introduction

Water is a fundamental resource that ensures the survival of all living things on the earth (Schellekens et al. 2018). But, nowadays, access to clean and improved water is becoming a great pressing issue because of the increasing environmental pollution that results from the rapid growth of industrialization and urbanization (Fu et al. 2015). The major causes of water pollution are different kinds of organic and inorganic pollutants caused by various industrial wastes, and natural and anthropogenic factors (Quiton et al. 2021). Inorganic contaminants are the compounds of inorganic by-products, such as fluoride, halide, iron, nitrate, etc., and persist longer in an aqueous system, do not degrade easily, and cause further deterioration (Srivastav and Ranjan 2020). Organic contaminants also include different compounds of pesticides, veterinary products, pharmaceuticals, personal care products, industrial compounds/by-products, engineered nanomaterials, food additives, and organic dyes (Mahmood et al. 2022). In particular, synthetic organic dyes and pigments discharged by industries such as textiles, paints, printing inks, cosmetics, plastics, and paper cause significant environmental pollution because of their hydrophilic nature, complex aromatic structure, and high stability against water, light, chemicals, temperature, etc. (Liu et al. 2018). In addition, synthetic dyes seriously affect human health and the environment due to their toxicity, long persistent, teratogenic, carcinogenic, and mutagenic properties (Abay et al. 2017). Hence, the reduction and elimination of toxic organic contaminants are very critical (Tian et al. 2016, 2020).

So far, various strategies such as biological processes (aerobic and anaerobic degradation), physical/traditional processes (adsorption, membrane filtration, and flocculation), and chemical process (photocatalytic degradation,

✉ Osman Ahmed Zelekew
osman.ahmed@astu.edu.et; osmax2007@gmail.com

[1] Department of Materials Science and Engineering, Adama Science and Technology University, 1888 Adama, Ethiopia

[2] Department of Materials Science and Engineering, National Taiwan University of Science and Technology, Taipei 10607, Taiwan

[3] College of Materials Engineering, Fujian Agriculture and Forestry University, Fuzhou 350002, China

[4] Department of Industrial Engineering, Universitas Prima Indonesia, Kota Medan, Indonesia

ozonation, Fenton-like reaction, electrochemical, and photochemical oxidation) have been developed and employed for such dye-containing wastewater (Hashimi et al. 2019; Kassem et al. 2021; Najeeb et al. 2021b; Saikia et al. 2017b; Swathi and Buvaneswari 2008; Zelekew et al. 2019). However, several constraints, such as discharge of massive amounts of sludge, low efficiency of dye removal, expensive recycling steps, release of non-degradable and toxic by-products into the environment, slow process, higher cost of materials, etc., limit the practical utility of this technique (Abay et al. 2017; Benhadria et al. 2022; Singh et al. 2014; Sun et al. 2019b). Among all those techniques, the catalytic reduction of organic dye is the most advanced technology due to several reasons (Begum et al. 2020). It is an easy operation, high efficiency, and low-cost process. In addition, harmful dyes are converted to useful by-products that can be employed as precursors or raw materials in a variety of industries (Kong et al. 2017). This technique is not only a quick process, but it also achieves total dye removal, making it preferable to the oxidative degradation process, which only achieves incomplete dye removal. Furthermore, the recycling procedures for the catalysts used for reduction reactions are simple and straightforward (Swathi and Buvaneswari 2008; Zelekew et al. 2019). This also suggests that the catalytic reduction is more cost-effective than the conventional adsorption technique, which requires lengthy separation procedures and additional setups to remove the adsorbed dye from the catalyst (Najeeb et al. 2021a).

The catalytic reductive degradation of organic dyes in the presence of sodium borohydride ($NaBH_4$) occurs by the electron transfer mechanism (Kassem et al. 2021). In the absence of an effective catalyst, the reduction of dye is thermodynamically favorable, but there is a significant kinetic barrier between the electron donor BH_4^- ion and acceptor dyes, which might obstruct the electron transport (Hashimi et al. 2019). The catalysts, surprisingly, are capable of reducing the potential difference due to their high Fermi potentials, which allow them to degrade dyes efficiently (Saikia et al. 2017a). As a result, designing and synthesizing catalytic materials with appropriate redox potential between the electron donor and acceptor species to operate as an efficient electron relay system is very crucial (Saikia et al. 2017a).

To date, several catalysts have been produced for the removal of such pollutants, including zeolites, noble metal nanoparticles such as Au, Ag, Pt, Pd, metal oxides, ferrites, and composite materials (Singh et al. 2014). Noble metal nanoparticles are well-known catalysts in the reduction reactions and have piqued the interest of researchers for a long time due to their effective catalytic activity; however, the high manufacturing costs of these materials limit their usage as catalysts in large-scale applications (Benhadria et al. 2022). Thus, the investigation of inexpensive, environmentally friendly, and efficient catalysts is still the main concern for researchers (Sun et al. 2019a).

Bimetallic catalysts have better catalytic potential than their individual metal (monometallic equivalents), because of the synergistic effects between two metals and the degree of freedom that may be modified to boost the catalytic efficiency of bimetallic nanomaterials (Naz et al. 2021). The increased efficiency of the bimetallic catalyst is commonly related to the electronic interactions between the two metals at the metal/metal interfaces. One metal will attract electrons from the active species, causing its d-electron density to change and facilitating effective catalysis (Alshammari 2018). The interatomic distances between the metal atoms can be changed by changing the properties of the electron orbitals, which is significant in improving catalytic efficiency and leading to enhanced catalysis compared to metal nanoparticles (Alshammari 2018). Nowadays, bimetallic oxysulfide catalysts have been employed for the treatment of water pollutants due to their facile, green, and economic preparation technique, and effective catalytic performance. Abdeta et al. synthesized a novel AgMoOS oxysulfide catalysts and effectively reduced chromium (VI) and organic dyes such as methylene blue, methyl orange, rhodamine blue, and 4-nitrophenol under dark conditions (Abdeta et al. 2021). Wu et al. synthesized a wool-coiled MoSrOS oxysulfide catalyst for the reduction of heavy metal ions and organic pollutants (Wu et al. 2021b). Jiang et al. prepared oxygen vacancy-rich bismuth oxysulfide (Bi_2O_2S) for effective photocatalytic reduction of CO_2 to CH_4 under visible light irradiation (Jiang et al. 2021). Re et al. synthesized cobalt-doped bismuth oxysulfide (Co-doped Bi_2O_2S) for catalytic degradation of tetracycline through peroxymonosulfate activation (Ren et al. 2021). Tadesse et al. synthesized vanadium-doped $Mo(O,S)_2$ oxysulfide for enhanced photocatalytic degradation of methylene blue dye under visible light irradiation (Tadesse et al. 2020). Tadesse et al. also synthesized $Nd_2O_3/Mo(S,O)_{3-x}{\cdot}0.34H_2O$ heterojunction for efficient photocatalytic degradation of rhodamine blue, methylene blue, and methylene orange (Tadesse et al. 2021). Nishioka et al. synthesized zinc-based oxysulfide $SrZn_2S_2O$ photocatalyst for reduction and oxidation of water under bandgap irradiation (Nishioka et al. 2019). Ni–Mn bimetallic oxide ($NiMn_2O_4$) was also fabricated as electrocatalysts for Al-air batteries and reported that it had excellent ORR catalytic performance (Deng et al. 2021). Ni-Mn bimetallic oxide nanosheets synthesized on carbon cloth substrate were also reported as a high-performance electrode for asymmetric supercapacitors (Tang et al. 2019). Cao and his coworkers also reported bimetallic Ni-Mn sulfides as very electrochemical active materials for supercapacitors with promising electrochemical performance, and their activity can be tuned by varying the molar ratio of Ni to Mn (Cao et al. 2018). However, there is no report on the synthesis

of bimetal nickel manganese oxysulfide (NiMnOS) catalyst prepared in a water bath for reduction of MB dye.

Herein, the novel nickel manganese oxysulfide (NiMnOS) catalysts were synthesized with facile preparation technique at low temperature with varying molar ratio of Ni:Mn in water bath. The bare NiOS and MnOS were also prepared for comparison purposes. The resulting catalysts were characterized using XRD, XPS, SEM/EDS, FT-IR, PL, and UV–Vis spectroscopy. The catalytic activity of the as-synthesized catalysts was evaluated by the reduction of methylene blue dye in the presence of $NaBH_4$. Furthermore, the stability and reusability of best catalyst were examined. Finally, a possible reduction mechanism with NiMnOS catalyst was proposed. It is expected that the bimetallic catalyst will exhibit high catalytic performance due to the synergetic effect of the two metals.

Materials and methods

Chemicals

Manganese (II) sulfate monohydrate [$MnSO_4.H_2O$, Alpha Chemika, 98%], nickel acetate tetrahydrate [$Ni(CH_3COO)_2.4H_2O$, Loba Chemie, 98%], thiourea [CH_4N_2S, Finkem], sodium borohydride [NaBH4, Alpha Chemika, 97%], methylene blue [MB, SDFCL], ethanol, and distilled water were used throughout the experiment. All of the chemicals were of analytical grade and used without further purification.

Synthesis of NiMnOS catalyst

To fabricate NiMnOS catalysts, nickel acetate tetrahydrate, manganese (II) sulfate monohydrate, and thiourea were used as nickel, manganese, and sulfur sources, respectively. The synthesis method was adopted from the previous study (Li et al. 2021b) with modifications. The NiMnOS catalysts were obtained through a facile solution-based process with varying molar ratios of Ni and Mn to study if the metal composition affects the methylene blue reduction performance. The bimetallic NiMnOS catalyst was prepared as follows. In a typical synthesis, 10 mmol of $Ni(CH_3COO)_2.4H_2O$ was dispersed in 400 mL of distilled water under magnetic stirring at room temperature and a light green solution was formed. Then, 30 mmol of $MnSO_4.H_2O$ was added to the solution under vigorous stirring. Subsequently, 40 mmol of thiourea was added to the above mixture and stirred for 30 min. The aforementioned mixture was transferred into water bath and reacted for 5 h at 90 °C. After the reaction was completed, the solution was naturally cooled to room temperature and centrifuged to obtain the precipitate. The collected precipitate was washed with distilled water and ethanol. Finally, it was dried in an oven at 80 °C for 12 h. After being dried, the resulting precipitate from Ni: Mn molar ratio of 25:75 was abbreviated as NiMnOS-25. The other samples, with Ni: Mn molar ratios of 50:50 and 75:25, were also prepared with the similar procedure described above and denoted as NiMnOS-50 and NiMnOS-75, respectively. For comparison, MnOS and NiOS catalysts were prepared using the same approach. Scheme 1 shows the schematic procedure for the synthesis of NiMnOS-25 catalyst.

Catalyst characterization

The phase purity and crystal structure of the as-synthesized samples were examined by using powder X-ray diffraction (XRD) (SHIMADZU XRD-7000). The X-ray photoelectron spectroscopy (XPS) studies were conducted using an ESCALAB 250 photoelectron spectrometer. The surface morphology and elemental analysis of the as-prepared samples were analyzed by scanning electron microscopy (SEM) equipped with energy-dispersive X-ray spectroscopy (EDS) (JSM 6500F, JEOL). Functional group examination was carried out by Fourier transform infrared (FT-IR) spectra (Spectrum 65 FT-IR, Perkin Elmer) using KBr pellets. Photoluminescence (PL) emission spectrum was performed using the Cary Eclipse fluorescence spectrometer (G9800A) at room temperature with the excitation wavelength of 325 nm. Ultraviolet–visible (UV–Vis) absorption of the catalyst samples and concentration of methylene blue were examined using UV–Vis spectroscopy (Shimadzu–3600 Plus).

Catalytic reduction performance evaluation

The catalysts were tested for the reduction of MB dye in aqueous solution. Specifically, 30 mg of $NaBH_4$ was added into 100 mL (10 ppm) of MB solution under stirring. Then, 30 mg of NiMnOS catalyst was added into the mixture to start the reduction reaction. The methylene blue reduction reaction was carried out at room temperature. The color of the mixture gradually changed from blue to colorless, indicating that the reduction reaction had been conducted. The concentration of MB was monitored at time interval of 1 min by using UV–Vis spectrophotometer. The degradation efficiency of the above reaction was calculated according to Beer–Lambert's law (Eq. 1) (Xia et al. 2019).

$$D(\%) = \left(\frac{A_0 - A_t}{A_0}\right) \times 100 \quad (1)$$

where A_0 represented the initial absorbance of the substrate solution and A_t represented the absorbance of the substrate solution at various time intervals.

The stability and reusability of the best catalyst (NiMnOS-25) catalyst were also tested. Particularly, 150 mg of

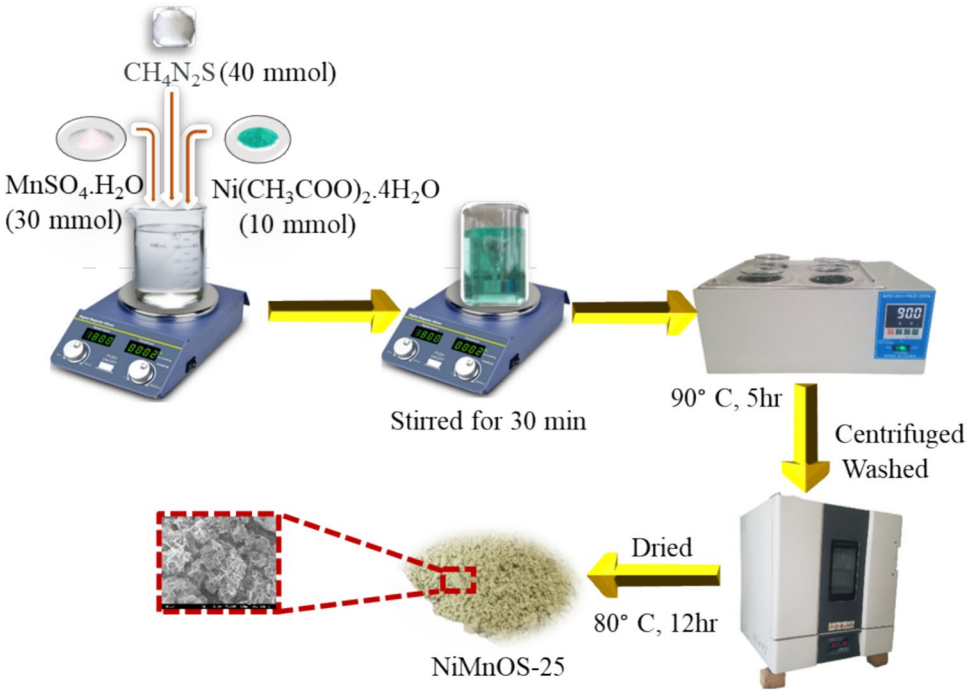

Scheme 1 The schematic diagram for the synthesis of the NiMnOS-25 catalyst

$NaBH_4$ has been added into 500 mL of MB (10 ppm) aqueous solution. Then, 150 mg of NiMnOS-25 catalyst was added under stirring. The reduction of MB solution was determined by using UV–Vis spectrophotometer. After the first round was completed, the resulting solution was made to settle and the upper layer of the solution was removed. Then, the remaining solution with the catalyst was centrifuged and washed with water and ethanol. Finally, the powder was dried in an oven at 80 °C for 12 h. The dried powder was utilized in the second run experiment using the same procedure as the first. The third and fourth runs also followed a similar pattern as stated in the first round.

Results and discussion

X-ray diffraction was used to assess the overall crystallinity catalysts. Figure 1 shows the XRD diffraction patterns of the as-synthesized NiOS, NiMnOS-75, NiMnOS-50, NiMnOS-25, and MnOS samples. The XRD pattern of NiOS (Fig. 1a) showed that the main diffraction peaks at 2θ value of 12.14°, 24.44°, 33.28°, 36.94°, 59.4°, and 70° corresponds to (001), (002), (110), (111), (300), and (220) planes, respectively, and indicated the hexagonal $Ni(OH)_2.2H_2O$ (JCPDS No.00–022-0444). The diffraction patterns of NiMnOS-75 (Fig. 1b), NiMnOS-50 (Fig. 1c), and NiMnOS-25 (Fig. 1d) indicate a broad peak of $Ni(OH)_2.2H_2O$ with lower intensity. In addition, the marginal shift of XRD peaks to lower angles was also observed, which shows that the addition of Mn did change the original phase of the material.

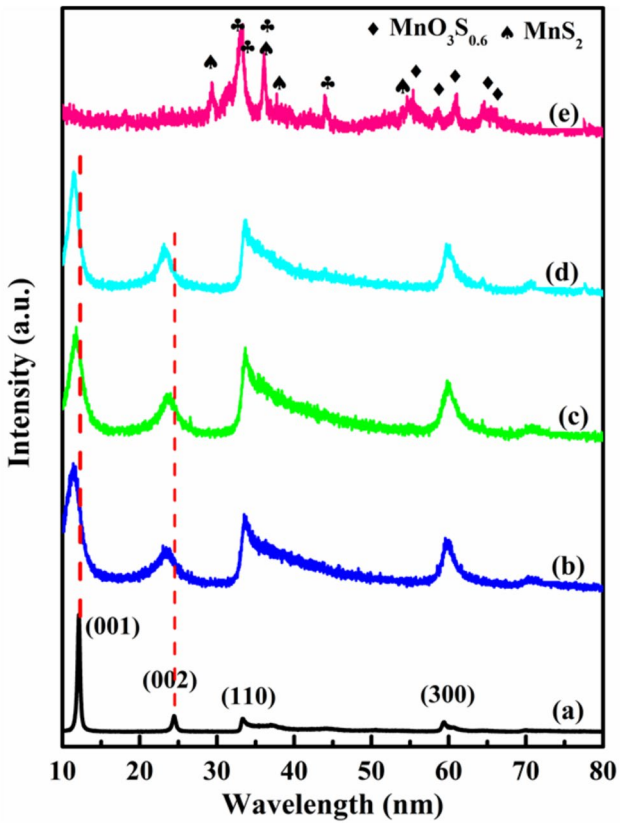

Fig. 1 X-ray diffraction pattern of **a** NiOS, **b** NiMnOS-75, **c** NiMnOS-50, **d** NiMnOS-25, and **e** MnOS

These peak shifts in the XRD may be due to the change in the crystal lattice which is caused by the incorporation of Mn, a higher ionic radius, into Ni sites. The decrease in diffraction intensity is also indicated that the crystallinity of the material is decreased due to the addition of manganese. In addition, the low synthesis temperature below 100 °C may result in poor crystallization and nanopowder size which is contributed to the weakening and broadening of NiMnOS peaks (Chen et al. 2019b). There were no further secondary phases found, indicating that the as-prepared NiMnOS catalyst is a solid solution-type single phase. The bare MnOS (Fig. 1e) showed poor crystallinity with the main diffraction peaks at 2θ of 32.9°, 33.9°, 36.02°, 43.4°, 55.2°, 58.6°, 60.4°, 64.3°, and 65.7° corresponds to the $MnO_3S_{0.6}$ (JCPDS card no. 00–021-0556). The diffraction peaks observed at 2θ of 29.3°, 33.2°, 36.1°, and 54.7° can be also ascribed to the (200), (210), (211), and (023) planes of cubic MnS_2 (JCPDS card no. 01–076-2047).

The chemical binding energy of the as-synthesized NiMnOS-25 catalyst was investigated using XPS analysis. As shown in Fig. 2a, the two major peaks with binding energies at 872.75 and 855.1 eV, represent the Ni $2p_{1/2}$ and Ni $2p_{3/2}$ levels, respectively. The Ni $2p_{1/2}$ and Ni $2p_{3/2}$ with the energy gap separation of 17.65 eV and the two satellite peaks located at 860.8 and 878.85 eV indicates the existence of Ni^{2+} in NiMnOS-25 (Yue et al. 2018). The Mn 2p XPS spectrum (Fig. 2b) showed that the peak of Mn 2p1/2 and Mn 2p3/2 located at 652.17 and 641.2 eV, respectively, with the separation energy gap of 10.97 eV, indicate the existence of Mn^{3+} ions. The peak position at 644.9 and 654.05 eV also ascribed to Mn 2p3/2 and Mn 2p1/2 bands, respectively, correspond to Mn^{4+} ion (Chen et al. 2018; Xue et al. 2017). The O 1 s XPS spectra in the NiMnOS-25 catalyst showed (Fig. 2c) that the peaks at 531 eV and 530 eV corresponds to the hydroxyl oxygen and the lattice oxygen, respectively (Sun et al. 2019b). Moreover, the S 2p XPS spectra of NiMnOS are also displayed in Fig. 2d. The S 2p peaks at a binding energy of 168.55 eV belong to S^{6+} (Chen et al. 2019a) and at 167.2 eV show the S–O bonding with sulfate features (Tang et al. 2017).

The morphology of the as-synthesized NiOS, MnOS, and NiMnOS-25 catalysts was investigated using scanning electron microscope (SEM) as shown in Fig. 3. As it is observed from Fig. 3a, bare NiOS shows a sheet-like

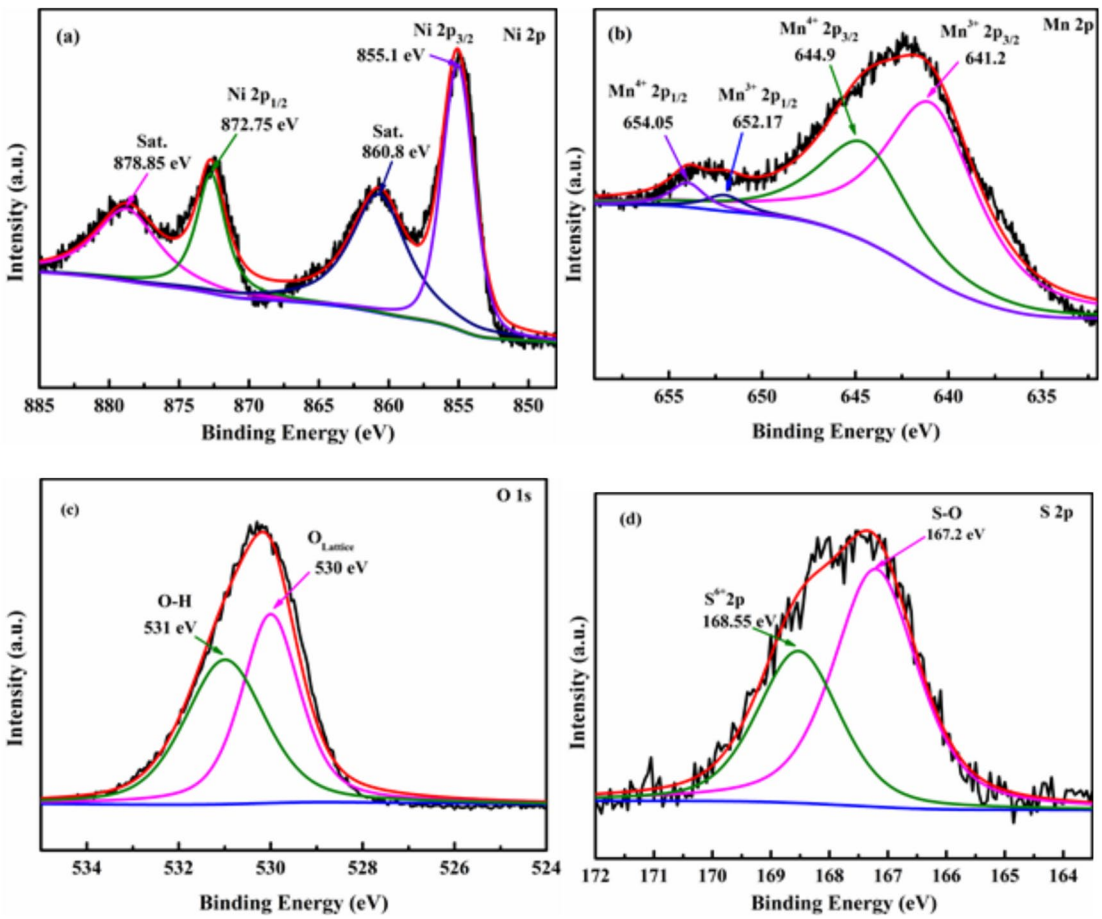

Fig. 2 XPS spectra of **a** Ni 2P, **b** Mn 2p, **c** O 1 s, and **d** S 2p in the NiMnOS-25

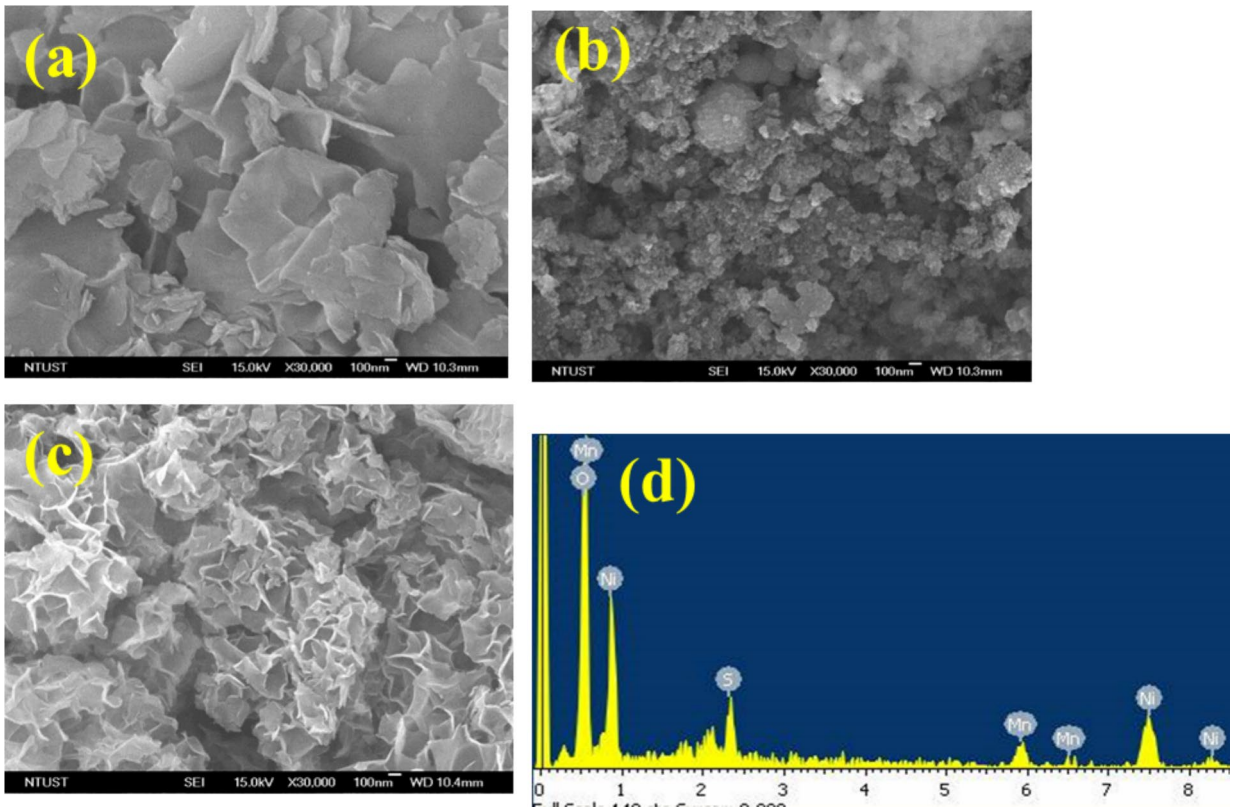

Fig. 3 SEM images of **a** NiOS, **b** MnOS, and **c** NiMnOS-25, and **d** the EDS spectrum of NiMnOS-25 catalyst

structure with a larger size. Moreover, the morphology of the MnOS is shown in Fig. 3b and exhibits aggregated nanoparticles with various sizes ranging from smaller to bigger particles size. Figure 3c shows the NiMnOS-25 catalyst and exhibited a sheet-like structure with a smaller size and uniform morphology. The sheet-like shape in the structure has more space and open channels, which provides more interaction sites for reduction reactions to occur. The elemental composition of the as-synthesized catalyst was also checked by using energy-dispersive X-ray spectroscopy (EDS). Figure 3d shows the elemental analysis of as-prepared NiMnOS-25. As it is indicated in Fig. 3d, the presence of nickel (Ni), manganese (Mn), oxygen (O), and sulfur (S), showed the successful synthesis of bimetallic NiMnOS oxysulfide catalysts.

The UV–Vis absorption spectra of NiMnOS catalysts prepared with various molar ratio of Ni:Mn are shown in Fig. 4a. It was observed that with increasing the Mn content, the bimetallic NiMnOS oxysulfide had better absorbance of visible light. The samples exhibit a broad wavelength absorption range, indicating that the sample band has more absorption states or defects. The direct bandgap (*Eg*) of the samples was calculated from UV–Vis absorption spectra by using the standard Tauc method (Sharrouf et al. 2015).

$$(\alpha hv)^2 = k(hv - Eg) \tag{2}$$

where $\alpha = 2.303\ A/L$, A is the absorbance of the sample and L is the path length (1 cm), h is the Planck constant, k is the absorption constant for direct transition, hv is the absorption energy, and Eg is the bandgap. Figure 4b shows the $(\alpha hv)^2$–hν curves of NiMnOS catalysts prepared with different Ni:Mn molar ratio, together with NiOS and MnOS. The bandgaps of NiOS, NiMnOS-75, NiMnOS-50, NiMnOS-25, and MnOS were obtained as 3.94, 3.54, 3.28, 2.37, and 2.57 eV, respectively. It is observed that the Eg value of bimetallic NiMnOS decreased when the amount of Mn increased. Compared with the bandgap value of NiO at 3.6–4 eV (Shi et al. 2021), MnO at 3.6–4.2 eV (Lim et al. 2016), MnO_2 at 1.3 eV (Cockayne and Li 2012), NiS at 0.9 eV (Addawiyah and Gunlazuardi 2018), MnS at 3.1 eV (Chaki et al. 2017), the variation of bandgap energy values shows that NiMnOS is a bimetal oxysulfide in the form solid solution (Chen et al. 2019b).

Fourier transform infrared (FT-IR) studies were conducted in the range of 4000–400 cm^{-1} to identify the functional groups of the as-prepared samples as shown in Fig. 5. The broad peak in the range of 3000–3700 cm^{-1} relates to the O–H stretching vibrations of hydroxyl groups and the interlayer water molecules in the structure (Zhang et al.

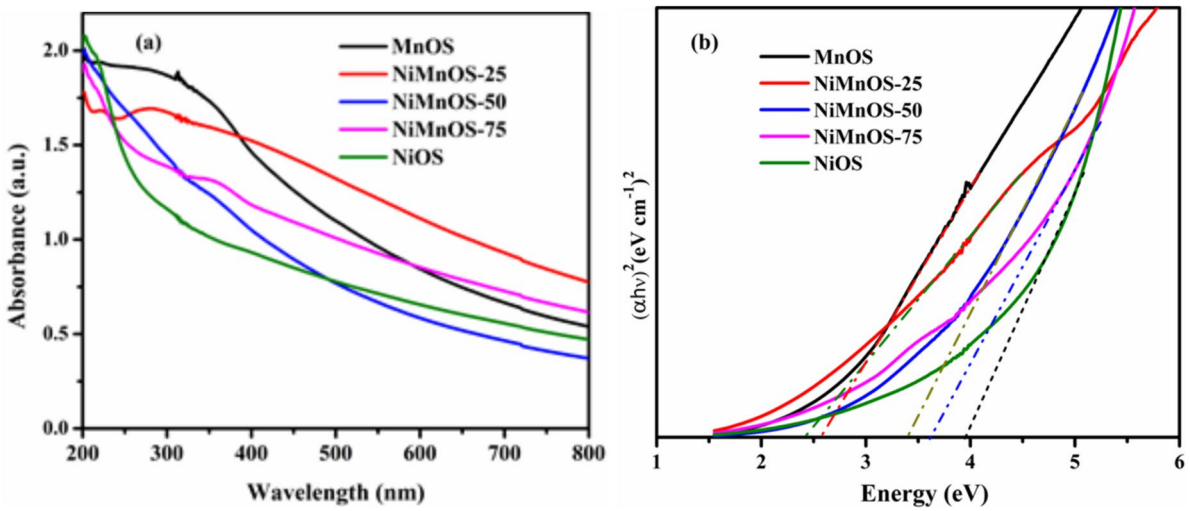

Fig. 4 **a** UV–Vis absorption spectra, **b** the $(\alpha h\nu)^2$-hν plot from the UV–Vis absorption of NiMnOS catalysts prepared with different molar ratio of Ni:Mn

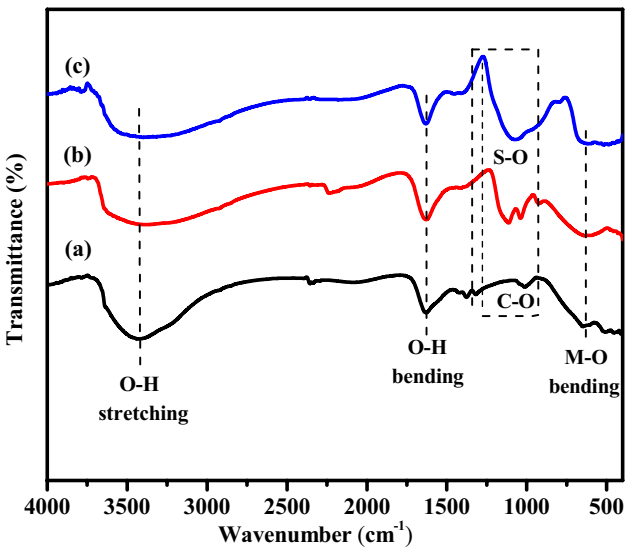

Fig. 5 FT-IR spectra of **a** NiOS, **b** NiMnOS-25, and **c** MnOS

2021). The broadening of the band is due to the formation of hydrogen bonds (Taibi et al. 2002). The band at 1630 cm^{-1} was ascribed to the bending vibration mode of interlayer water molecules (Wu et al. 2013). The band around 1012 cm^{-1}, in Fig. 5a, is occurred due to the stretching vibration of C–O bond (Baruah et al. 2019; Jansi Rani et al. 2019). As shown in Fig. 5c, the intense band at 1068 cm^{-1} displayed the presence of S–O bond due to the SO_3^- group from Mn source precursor (Oriakhi et al. 1996; Poul et al. 2000). In Fig. 5b the peak shift to the higher wavenumber is observed in the case of NiMnOS-25, which implies the incorporation of Mn. In addition, both C–O and S–O bonds were observed at 1038 cm^{-1} and 1112 cm^{-1}, respectively. The band around 638 cm^{-1} is associated with the bending mode of M–O bond (Mn–O, Ni–O), and the band below 500 cm^{-1} can be due to the stretching vibration of M–O bond (Dong et al. 2019; Li et al. 2017).

The performance of the catalyst was assessed with the reduction of MB dye in an aqueous solution. Figure 6 indicates the catalytic performance of the NiMnOS catalysts toward the reduction of MB to Leuco-methylene blue (LMB) in the presence of $NaBH_4$. The catalytic reduction reaction was carried out at room temperature under ambient conditions. In the reduction process, the nucleophile BH^{4-} can donate electrons to the catalyst, and the electrophile MB can receive electrons from the catalyst. Thus, in a $NaBH_4$ solution, the catalyst acts as an electron relay for MB reduction.

The catalytic reduction of MB was studied with only the $NaBH_4$ and without catalyst, and with the catalyst and without $NaBH_4$. As shown in Fig. 6a, with the addition of only $NaBH_4$ into MB solution, the intensity of MB peak at absorption maxima of $\lambda_{max} = 664$ nm almost stayed unchanged even for a long time, indicating that the reduction process of MB does not occur in the absence of any catalysts with $NaBH_4$ (Shi et al. 2016). The reduction of MB into Leuco-methylene blue (LMB) is thermodynamically feasible with only $NaBH_4$; however, large energy barrier between two reactant species prevents the electron transfer from the BH_4^- donor to the MB acceptor (Hashimi et al. 2019). The reduction of MB was also not observed with only the catalyst in the absence $NaBH_4$ in the solution as shown in Fig. 6b. In the presence of both NiMnOS-25 catalyst and $NaBH_4$, the strong characteristic band of MB at 664 nm was found to diminish in about 5 min as shown in Fig. 6c. In order to further clarify the reduction of MB in aqueous solution by NiMnOS catalysts, the color variations before and after the

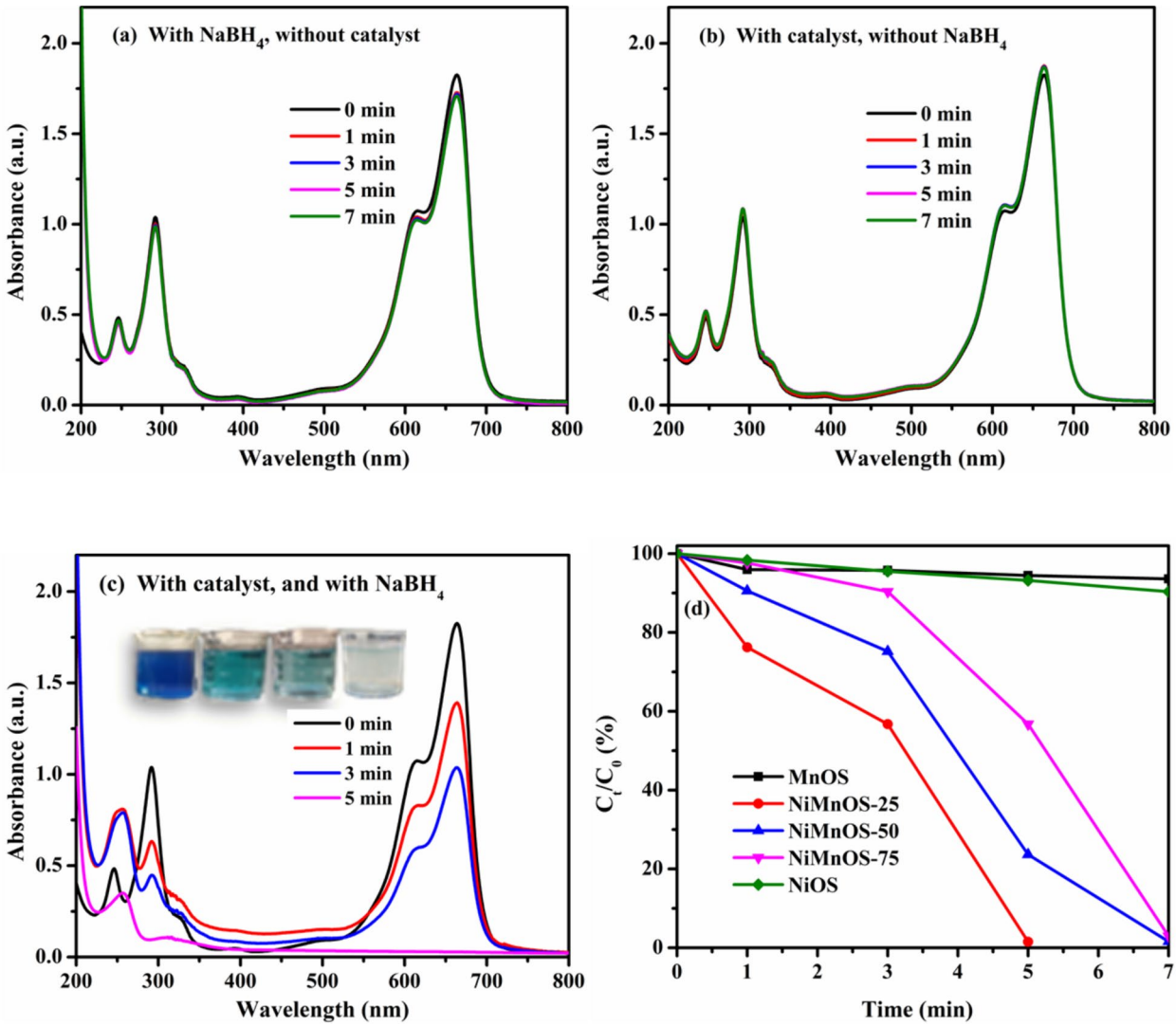

Fig. 6 Reduction of MB with **a** only $NaBH_4$, **b** only NiMnOS-25 catalyst, **c** NiMnOS-25 catalyst and with $NaBH_4$, **d** NiMnOS catalyst prepared at different molar ratio of Ni:Mn

reaction were observed. When both the catalyst and $NaBH_4$ are added to the MB solution for reaction, the test solution loses the blue color (MB) and finally becomes colorless, indicating that the MB solution has been eliminated. The course of the reaction has been tracked by using UV–Vis absorption spectrophotometry.

The Ct/Co ratio as a function of reaction time for the reduction of MB on MnOS, NiOS, and NiMnOS catalysts is shown in Fig. 6d. The MB reduction percentage of the catalyst follows the following order: NiMnOS-25 > NiMnOS-50 > NiMnOS-75 > NiOS > MnOS. The bimetallic NiMnOS-25 has the best catalytic performance among the prepared catalysts with a removal percentage of about 98.47% within 5 min, while the degradation percentage of bare NiOS is about 9.6% within 7 min. The higher reduction efficiency of the catalyst could be due to the higher metal loading in the bimetal catalyst than in the single metal catalyst, the presence of a strong synergetic effect between Ni and Mn atoms, and an increase in active sites of the catalyst (Abay et al. 2017). From the prepared bimetal NiMnOS catalysts, NiMnOS-25 has the highest catalytic performance, while NiMnOS-75 has the lowest. The lower performance of NiMnOS-75 may be attributed to the lower amount of Mn, which reduces the active sites in the catalyst and reduces catalytic efficiency (Li et al. 2021b; Zhang et al. 2011). As a result, the ideal molar ratio of Ni:Mn is 25:75, and the effectiveness of adding Mn to improve the catalyst's reduction performance has been proven.

The kinetic parameters of the borohydride-mediated MB reduction in the presence of nickel manganese oxysulfide (NiMnOS) catalyst were analyzed by measuring the change in dye concentration as a function of reaction time. In order

to obtain the catalytic apparent rate constant data of the MB reduction reaction, the kinetics of the catalytic reduction process can be fitted using the apparent first-order rate law. Figure 7a shows the linear fitting results for the NiOS, NiMnOS-75, NiMnOS-50, NiMnOS-25, and MnOS catalysts according to the apparent first-order rate equation expressed in Eq. (3)

$$\ln\left(\frac{C_t}{C_o}\right) = -kt \quad (3)$$

where C_t is the concentration of MB (ppm) at irradiation time t (min), C_o is the initial MB (mg/l) concentration, and k (min^{-1}) is the kinetic or apparent rate constant determined from the slope of the line.

The apparent rate constant for NiMnOS-25 catalyst was 65.3 $\times 10^{-2} min^{-1}$. However, the apparent rate constant values for the reduction of MB by using NiOS, NiMnOS-75, NiMnOS-50, and MnOS were 1.4 $\times 10^{-2} min^{-1}$, 33.1 $\times 10^{-2} min^{-1}$, 44.2 $\times 10^{-2} min^{-1}$, and 1.1 $\times 10^{-2} min^{-1}$, respectively. The specific rate constant, K, in terms of $min^{-1} g^{-1}$ was also measured. The NiMnOS-25 catalyst had the highest apparent rate constant of 21.8 $min^{-1} g^{-1}$. The kinetic rate constant of different catalysts was also studied as indicated in Table 1 and compared with other reported catalysts and showed comparable performance.

The stability and reusability of the bimetallic oxysulfide NiMnOS-25 catalyst were further investigated by monitoring the catalytic activity during repeated reduction reactions. As a result, the reusability of our catalyst was tested by the reduction of MB for 4 runs as shown in Fig. 8a. The result showed that, after 4 cycles, the bimetallic NiMnOS-25 oxysulfide catalyst maintained a good catalytic activity, which is above 96%, without deterioration. It is observed that the catalyst performs well on the following run, although it is

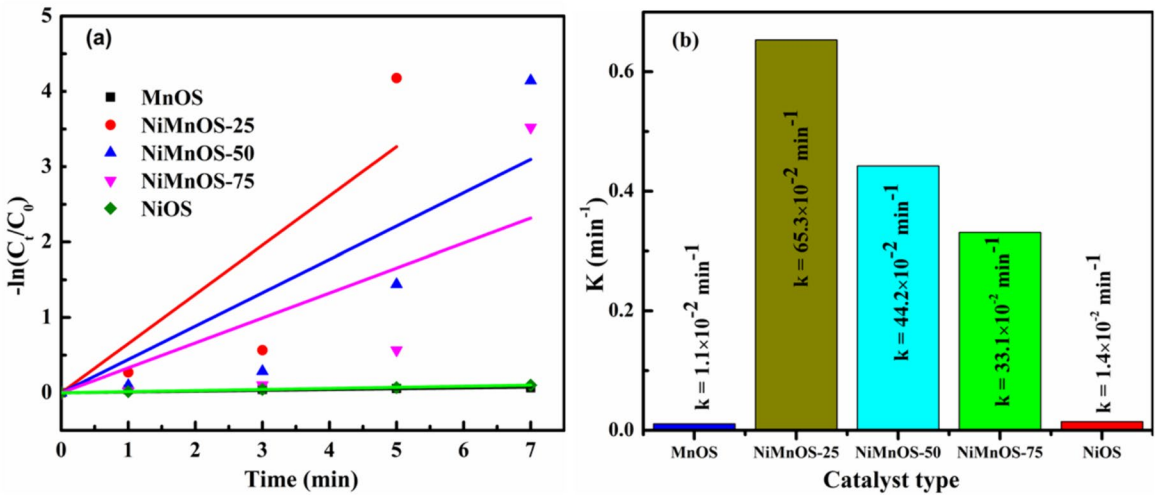

Fig. 7 **a** Plot of $-\ln(C_t/C_o)$ versus time for reduction of MB dye. **b** The kinetic rate constants for NiOS, NiMnOS-75, NiMnOS-50, NiMnOS-25, and MnOS catalysts

Table 1 The kinetic rate constant of the catalysts for degradation of methylene blue

Catalysts	Time (min)	Kinetic rate constant, K_{app} (10^{-2} min^{-1})	Specific rate constant, K ($min^{-1} g^{-1}$)	References
$Ag/Fe_3O_4@C$	10	0.34	0.034	Zhu et al. (2013)
Au/TiO_2	12	0.156	0.078	Khan et al. (2014)
$CuVOS@SiO_2$	2	0.435	87.0	Sun et al. (2020)
Sn/SnO_2	210	0.132	1.32	Das et al. (2018)
CuO-SDS	10	0.345	0.0345	Benhadria et al. (2022)
NiOS	7	1.4	0.48	This study
NiMnOS-75	7	33.1	11.03	This study
NiMnOS-50	7	44.2	14.74	This study
NiMnOS-25	5	65.3	21.8	This study
MnOS	7	1.1	0.36	This study

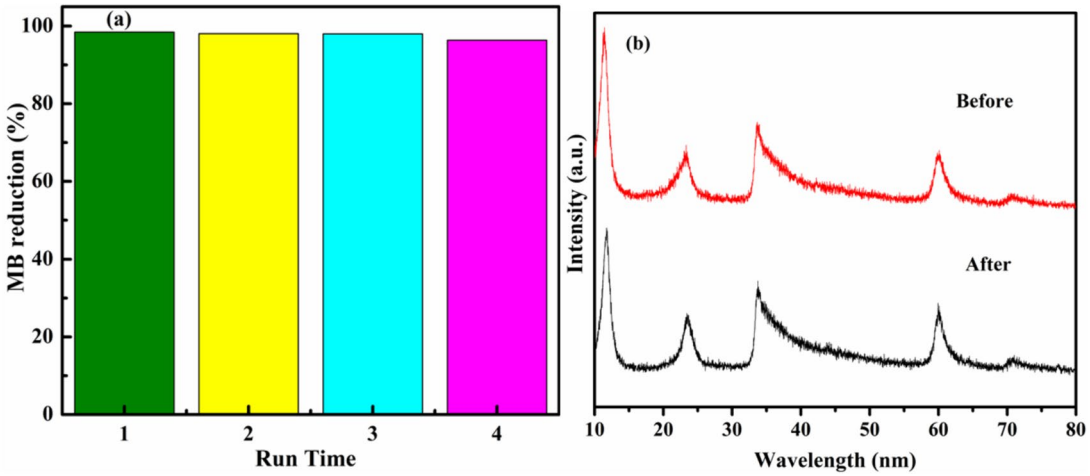

Fig. 8 **a** Reusability of NiMnOS-25 catalyst for the reduction of MB, **b** XRD pattern of NiMnOS-25 before and after four cycles

not as excellent as the first cycle. As the number of recycling increases, the catalyst's catalytic activity declines. The slight decrease in the performance of the catalyst is attributed to the loss of the catalyst during the recycling process. Furthermore, after the fourth catalytic cycle of the reduction of MB, XRD analysis of the catalyst was performed to determine its stability. The XRD patterns of NiMnOS-25 before and after four cycles of MB reduction are shown in Fig. 8b. As compared to the fresh catalyst, no recognizable differences were noticed. The structure and crystalline phase of the NiMnOS-25 catalyst remained unchanged following catalytic reduction, indicating that it is stable during the reduction process and suitable for practical applications.

According to the above-mentioned results and earlier works (Kumar and Deka 2014; Wu et al. 2021a), a possible catalytic reaction mechanism for the reduction of methylene blue (MB) to Leuco-methylene blue (LMB) in the presence of $NaBH_4$ over a NiMnOS-25 catalyst was proposed as shown in Fig. 9. First, $NaBH_4$ is dissociated in an aqueous solution and generated borohydride ions (BH_4^-). The BH_4^- ion was then adsorbed and transferred hydride ions to the surface of the catalyst (Guo et al. 2020). The hydride ions produced from $NaBH_4$ formed covalent bond with the metal ions on the surface of the NiMnOS catalysts (Chen et al. 2019c). Subsequently, the adsorption of methylene blue (MB) on the surface of the catalyst has occurred, and strong interactions between adsorbed MB and hydride ions are formed. The reduction of MB occurred via electron relay from donor species (H^-) to acceptor MB (Sun et al. 2020). Furthermore, as shown by the XPS analysis, the presence of Mn^{3+}, Mn^{4+}, and Ni^{2+} ions in NiMnOS catalysts boosts electron transport and accelerates the reduction activity (Abdeta et al. 2021; Li et al. 2021a). Finally, due to the decreased electrostatic interaction between the catalyst and Leuco-methylene blue, the desorption of LMB from the surface of the NiMnOS-25 catalyst will spontaneously occur, resulting in a free surface for the next catalytic reduction cycle to take place (Hu et al. 2019). Here, the catalyst serves two different purposes (Chen et al. 2019b, 2019c): The first is to provide an interaction center with $NaBH_4$ and organic dyes for orientation-controlled electrophilic and nucleophilic reactions; the second is to act as an electron conductor through electron transfer mechanism between Mn^{3+}/Mn^{4+}. Therefore, the reduction reaction is achieved due to both the catalyst and $NaBH_4$, which are used to release the electron and hydride ions, respectively.

Conclusion

The NiMnOS catalyst was prepared via a facile and environmentally friendly technique. The prepared catalysts were characterized, and the catalytic efficiency toward the reduction of methylene blue dye was examined. The reduction reaction results showed that the catalyst prepared with a Ni:Mn molar ratio of 25:75 (NiMnOS-25) had the best catalytic activity and reduced 98.46% of MB within 5 min. However, NiOS, NiMnOS-50, NiMnOS-75, and MnOS were reduced 9.6%, 98.41%, 97.04%, and 6.40% of MB within 7 min, respectively. The NiMnOS catalyst showed higher reduction efficiency in comparison with the corresponding NiOS and MnOS due to the synergetic effects of the two metals. The presence of Mn in the NiOS catalyst assists the electron relay and provides more active sites for the reduction reaction. A good stability and reusability of NiMnOS-25 catalyst were also observed after four cycles of reduction reaction. Hence, the novel NiMnOS catalyst could have a promising application in the wastewater treatment

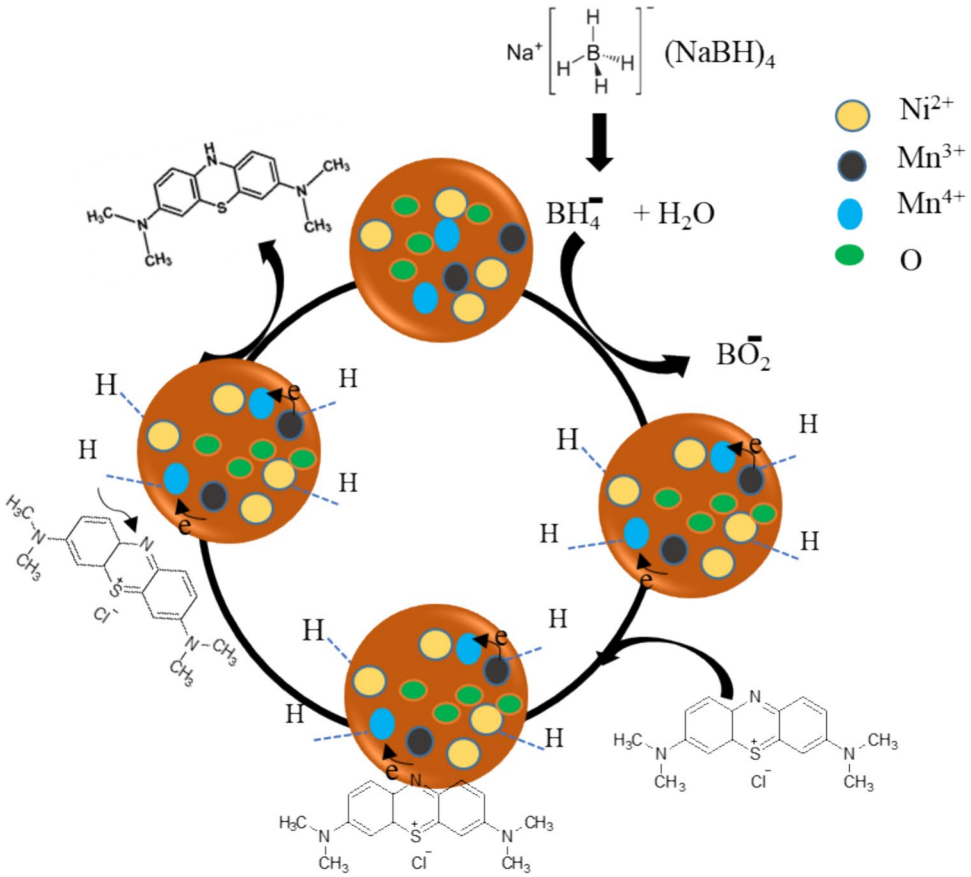

Fig. 9 Proposed reduction reaction mechanism of MB in the presence of the NiMnOS catalyst

technology targeting colored pollutants in the dye manufacturing and textile industries.

Acknowledgements We would like to acknowledge Adama Science and Technology University (ASTU) for supporting this MSc. thesis work under the Grant No. ASTU/SM-R/437/22. We also acknowledged the National Taiwan University of Science and Technology (NTUST) for SEM/EDS and XPS analysis.

Funding The authors did not receive funds from any funding organization. However, Adama Science and Technology University (ASTU) covered laboratory expenses and other costs for this MSc. Student thesis work.

Declarations

Conflict of interest The authors declare no competing interest.

Ethical approval The authors declare no any ethical conduct.

References

Abay AK, Kuo D-H, Chen X, Saragih AD (2017) A new V-doped Bi2 (O, S) 3 oxysulfide catalyst for highly efficient catalytic reduction of 2-nitroaniline and organic dyes. Chemosphere 189:21–31

Abdeta AB, Sun H, Guo Y, Wu Q, Zhang J, Yuan Z, Lin J, Chen X (2021) A novel AgMoOS bimetallic oxysulfide catalyst for highly efficiency catalytic reduction of organic dyes and chromium (VI). Adv Powder Technol 32(8):2856–2872

Addawiyah E and Gunlazuardi J (2018) Nickel sulfide sensitized TiO2 nanotubes system as photo-anode: will this system active under visible light and why?, p 020090, AIP Publishing LLC.

Alshammari K (2018) Heterogeneous catalysis using supported metal nanoparticles for environmental applications. Cardiff University.

Baruah JM, Kalita S, Narayan J (2019) Green chemistry synthesis of biocompatible ZnS quantum dots (QDs): their application as potential thin films and antibacterial agent. Int Nano Lett 9(2):149–159

Begum R, Najeeb J, Sattar A, Naseem K, Irfan A, Al-Sehemi AG, Farooqi ZH (2020) Chemical reduction of methylene blue in the presence of nanocatalysts: a critical review. Rev Chem Eng 36(6):749–770

Benhadria N, Hachemaoui M, Zaoui F, Mokhtar A, Boukreris S, Attar T, Belarbi L, Boukoussa B (2022) Catalytic reduction of methylene blue dye by copper oxide nanoparticles. J Cluster Sci 33(1):249–260

Cao J, Yuan S, Yin H, Zhu Y, Li C, Fan M, Chen H (2018) One-pot synthesis of porous nickel–manganese sulfides with tuneable compositions for high-performance energy storage. J Sol-Gel Sci Technol 85:629–637

Chaki SH, Chauhan SM, Tailor JP, Deshpande MP (2017) Synthesis of manganese sulfide (MnS) thin films by chemical bath deposition and their characterization. J Market Res 6(2):123–128

Chen H, Wu Z, Zheng Z, Chen T, Guo X, Li J, Zhong B (2018) Tuning the component ratio and corresponding sodium storage properties of layer-tunnel hybrid Na0. 6Mn1-xNixO2 cathode by a simple cationic Ni2+ doping strategy. Electrochim Acta 273:63–70

Chen X, Sun H, Zhang J, Guo Y, Kuo D-H (2019a) Cationic S-doped TiO2/SiO2 visible-light photocatalyst synthesized by co-hydrolysis method and its application for organic degradation. J Mol Liq 273:50–57

Chen X, Kuo D-H, Zhang J, Lu Q, Lin J (2019b) Nanosheet bimetal oxysulfide CuSbOS catalyst for highly efficient catalytic reduction of heavy metal ions and organic dyes. J Mol Liq 275:204–214

Chen X, Kuo DH, Zhang J, Lu Q, Lin J, Liao Y (2019c) Tubular bimetal oxysulfide CuMgOS catalyst for rapid reduction of heavy metals and organic dyes. Appl Organomet Chem 33(4):e4824

Cockayne E, Li L (2012) First-principles DFT+ U studies of the atomic, electronic, and magnetic structure of α-MnO2 (cryptomelane). Chem Phys Lett 544:53–58

Das O, Uddin M, Rahman M, Bhoumick M (2018) Highly active carbon supported Sn/SnO2 photocatalysts for degrading organic dyes. IOP Publishing, Bristol, p 012011

Deng J, Lu H, Xu B, Cao Y, Yang W, Liu J (2021) NiMn2O4-based Ni-Mn bimetallic oxides as electrocatalysts for the oxygen reduction reaction in Al–air batteries. Chem Eng J 413:127439

Dong B, Li W, Huang X, Ali Z, Zhang T, Yang Z, Hou Y (2019) Fabrication of hierarchical hollow Mn doped Ni (OH) 2 nanostructures with enhanced catalytic activity towards electrochemical oxidation of methanol. Nano Energy 55:37–41

Fu F, Cheng Z, Lu J (2015) Synthesis and use of bimetals and bimetal oxides in contaminants removal from water: a review. RSC Adv 5(104):85395–85409

Guo Y, Zelekew OA, Sun H, Kuo D-H, Lin J, Chen X (2020) Catalytic reduction of organic and hexavalent chromium pollutants with highly active bimetal CuBiOS oxysulfide catalyst under dark. Sep Purif Technol 242:116769

Hashimi AS, Nohan MANM, Chin SX, Zakaria S, Chia CH (2019) Rapid catalytic reduction of 4-nitrophenol and clock reaction of methylene blue using copper nanowires. Nanomaterials 9(7):936

Hu M, Yan X, Hu X, Feng R, Zhou M (2019) Synthesis of silver decorated silica nanoparticles with rough surfaces as adsorbent and catalyst for methylene blue removal. J Sol-Gel Sci Technol 89(3):754–763

Jansi Rani B, Dhivya N, Ravi G, Zance SS, Yuvakkumar R, Hong SI (2019) Electrochemical performance of β-Nis@ Ni (OH) 2 nanocomposite for water splitting applications. ACS Omega 4(6):10302–10310

Jiang L, Li Y, Wu X, Zhang G (2021) Rich oxygen vacancies mediated bismuth oxysulfide crystals towards photocatalytic CO2-to-CH4 conversion. Sci China-Mater 64(9):2230–2241

Kassem AA, Abdelhamid HN, Fouad DM, Ibrahim SA (2021) Catalytic reduction of 4-nitrophenol using copper terephthalate frameworks and CuO@ C composite. J Environ Chem Eng 9(1):104401

Khan MM, Lee J, Cho MH (2014) Au@ TiO2 nanocomposites for the catalytic degradation of methyl orange and methylene blue: an electron relay effect. J Ind Eng Chem 20(4):1584–1590

Kong X, Zhu H, Chen C, Huang G, Chen Q (2017) Insights into the reduction of 4-nitrophenol to 4-aminophenol on catalysts. Chem Phys Lett 684:148–152

Kumar M, Deka S (2014) Multiply twinned AgNi alloy nanoparticles as highly active catalyst for multiple reduction and degradation reactions. ACS Appl Mater Interfaces 6(18):16071–16081

Li H, Zhang H, Thayil S, Chang A, Sang X, Ma X (2021) Enhanced aging and thermal shock performance of Mn1. 95− xCO0. 21Ni0. 84SrxO4 NTC ceramics. J Adv Ceram 10(2):258–270

Li J, Wei M, Chu W, Wang N (2017) High-stable α-phase NiCo double hydroxide microspheres via microwave synthesis for supercapacitor electrode materials. Chem Eng J 316:277–287

Li X, Chen D, Li N, Xu Q, Li H, He J, Lu J (2021b) One-step fabrication of bimetallic CuCoOS as an efficient catalyst for Cr (VI) reduction. Environ Sci Nano 8(9):2453–2463

Lim JS, Saldana-Greco D, Rappe AM (2016) Improved pseudopotential transferability for magnetic and electronic properties of binary manganese oxides from DFT+ U+ J calculations. Phys Rev B 94(16):165151

Liu Y, Zhang Y, Kou Q, Chen Y, Han D, Wang D, Lu Z, Chen L, Yang J, Xing S (2018) Eco-friendly seeded Fe 3 O 4-Ag nanocrystals: a new type of highly efficient and low cost catalyst for methylene blue reduction. RSC Adv 8(4):2209–2218

Mahmood T, Momin S, Ali R, Naeem A and Khan A (2022) Technologies for removal of emerging contaminants from wastewater. In Wastewater Treatment, IntechOpen: Ch. 9, 1–20

Najeeb J, Ahmad G, Nazir S, Naseem K, Kanwal A (2021a) Critical analysis of various supporting mediums employed for the incapacitation of silver nanomaterial for aniline and phenolic pollutants: a review. Korean J Chem Eng 38(2):248–263

Najeeb J, Ahmad G, Nazir S, Naseem K, Kanwal A (2021b) Critical analysis of various supporting mediums employed for the incapacitation of silver nanomaterial for aniline and phenolic pollutants: a review. Korean J Chem Eng 38:248–263

Naz M, Rafiq A, Ikram M, Haider A, Ahmad SOA, Haider J, Naz S (2021) Elimination of dyes by catalytic reduction in the absence of light: a review. J Mater Sci 56(28):15572–15608

Nishioka S, Kanazawa T, Shibata K, Tsujimoto Y, zur Loye H-C and Maeda K (2019) A zinc-based oxysulfide photocatalyst SrZn2S2O capable of reducing and oxidizing water. Dalton Trans 48(42):15778–15781

Oriakhi CO, Farr IV, Lerner MM (1996) Incorporation of poly (acrylic acid), poly (vinylsulfonate) and poly (styrenesulfonate) within layered double hydroxides. J Mater Chem 6(1):103–107

Poul L, Jouini N, Fiévet F (2000) Layered hydroxide metal acetates (metal= zinc, cobalt, and nickel): elaboration via hydrolysis in polyol medium and comparative study. Chem Mater 12(10):3123–3132

Quiton KGN, Lu M, Huang YH (2021) Synthesis and catalytic utilization of bimetallic systems for wastewater remediation: a review. Chemosphere 262:128371

Ren J, Jiang L, Li Y, Zhang G (2021) Cobalt doped bismuth oxysulfide with abundant oxygen vacancies towards tetracycline degradation through peroxymonosulfate activation. Separat Purif Technol 275:119100

Saikia P, Miah AT, Das PP (2017a) Highly efficient catalytic reductive degradation of various organic dyes by Au/CeO 2-TiO 2 nanohybrid. J Chem Sci 129(1):81–93

Saikia P, Miah AT, Das PP (2017b) Highly efficient catalytic reductive degradation of various organic dyes by Au/CeO 2-TiO 2 nanohybrid. J Chem Sci 129:81–93

Schellekens J, Heidecke L, Nguyen N and Spit W (2018) The economic value of water–water as a key resource for economic growth in the EU. Rotterdam: ECORYS.

Sharrouf M, Awad R, Roumié M, Marhaba S (2015) Structural, optical and room temperature magnetic study of Mn 2 O 3 nanoparticles. Mater Sci Appl 6(10):850

Shi M, Qiu T, Tang B, Zhang G, Yao R, Xu W, Chen J, Fu X, Ning H, Peng J (2021) Temperature-controlled crystal size of wide band gap nickel oxide and its application in electrochromism. Micromachines 12(1):80

Shi Y, Zhang X, Zhu Y, Tan H, Chen X, Lu Z-H (2016) Core–shell structured nanocomposites Ag@ CeO 2 as catalysts for hydrogenation of 4-nitrophenol and 2-nitroaniline. RSC Adv 6(53):47966–47973

Singh C, Goyal A, Singhal S (2014) Nickel-doped cobalt ferrite nanoparticles: efficient catalysts for the reduction of nitroaromatic compounds and photo-oxidative degradation of toxic dyes. Nanoscale 6(14):7959–7970

Srivastav AL, Ranjan M (2020) Inorganic pollutants in water. Elsevier, Amsterdam, pp 1–15

Sun H, Zelekew OA, Chen X, Guo Y, Kuo D-H, Lu Q, Lin J (2019a) A noble bimetal oxysulfide CuVOS catalyst for highly efficient catalytic reduction of 4-nitrophenol and organic dyes. RSC Adv 9(55):31828–31839

Sun H, Zelekew OA, Chen X, Guo Y, Kuo D-H, Lu Q, Lin J (2019b) A noble bimetal oxysulfide Cu V OS catalyst for highly efficient catalytic reduction of 4-nitrophenol and organic dyes. RSC Adv 9(55):31828–31839

Sun H, Abdeta AB, Zelekew OA, Guo Y, Zhang J, Kuo D-H, Lin J, Chen X (2020) Spherical porous SiO2 supported CuVOS catalyst with an efficient catalytic reduction of pollutants under dark condition. J Mol Liq 313:113567

Swathi T, Buvaneswari G (2008) Application of NiCo2O4 as a catalyst in the conversion of p-nitrophenol to p-aminophenol. Mater Lett 62(23):3900–3902

Tadesse SF, Kuo D-H, Kebede WL, Duresa LW (2020) Synthesis and characterization of vanadium-doped Mo (O, S) 2 oxysulfide for efficient photocatalytic degradation of organic dyes. New J Chem 44(45):19868–19879

Tadesse SF, Kuo D-H, Kebede WL, Wolde GS (2021) Visible light driven Nd_2O_3/Mo (S, O) 3–x· 0.34 H_2O heterojunction for enhanced photocatalytic degradation of organic pollutants. Appl Surf Sci 569:151091

Taibi M, Ammar S, Jouini N, Fiévet F, Molinié P, Drillon M (2002) Layered nickel hydroxide salts: synthesis, characterization and magnetic behaviour in relation to the basal spacing. J Mater Chem 12(11):3238–3244

Tang Q, Li H, Zhang J, Lin Z, Pan Y, Hu Q, You Y, Ye Y (2017) A dual-faced interlayer prepared by electron beam evaporation for enhanced-performance lithium–sulfur batteries. RSC Adv 7(70):44035–44042

Tang X, Zhang B, Lui YH, Hu S (2019) Ni-Mn bimetallic oxide nanosheets as high-performance electrode materials for asymmetric supercapacitors. J Energy Storage 25:100897

Tian M, Dong C, Cui X, Dong Z (2016) Nickel and cobalt nanoparticles modified hollow mesoporous carbon microsphere catalysts for efficient catalytic reduction of widely used dyes. RSC Adv 6(101):99114–99119

Tian X, Liu M, Iqbal K, Ye W, Chang Y (2020) Facile synthesis of nitrogen-doped carbon coated Fe3O4/Pd nanoparticles as a high-performance catalyst for Cr (VI) reduction. J Alloy Compd 826:154059

Wu H-Y, Xie Y-L, Hu Z-A (2013) Synthesis, characterization and electrochemical properties of board-like Al-substituted alpha nickel hydroxides. Int J Electrochem Sci 8:1839

Wu Q, Wang X, Fu J, Zelekew OA, Abdeta AB, Kuo D-H, Zhang J, Yuan Z, Lin J, Chen X (2021) Wool-coiled bimetallic oxysulfide MoSrOS catalyst synthesis for catalytic reduction of toxic organic pollutants and heavy metal ions. J Sci Adv Mater Dev 6:578–586

Wu Q, Wang X, Fu J, Zelekew OA, Abdeta AB, Kuo D-H, Zhang J, Yuan Z, Lin J, Chen X (2021b) Wool-coiled bimetallic oxysulfide MoSrOS catalyst synthesis for catalytic reduction of toxic organic pollutants and heavy metal ions. J Sci Adv Mater Dev 6(4):578–586

Xia Y, Liu Y, Shi N, Zhang X (2019) Highly efficient reduction of 4-nitrophenolate to 4-aminophenolate by Au/γ-Fe 2 O 3@ HAP magnetic composites. RSC Adv 9(18):10272–10281

Xue Q, Pei Z, Huang Y, Zhu M, Tang Z, Li H, Huang Y, Li N, Zhang H, Zhi C (2017) Mn 3 O 4 nanoparticles on layer-structured Ti 3 C 2 MXene towards the oxygen reduction reaction and zinc–air batteries. J Mater Chem A 5(39):20818–20823

Yue D, Qian X, Ren M, Fang M, Jia J, Zhao Y (2018) Secondary battery inspired α-nickel hydroxide as an efficient Ni-based heterogeneous catalyst for sulfate radical activation. Sci Bull 63(5):278–281

Zelekew OA, Kuo D-H, Abdullah H (2019) Synthesis of (Sn, Zn)(O, S) bimetallic oxysulfide catalyst for the detoxification of Cr+ 6 in aqueous solution. Adv Powder Technol 30(12):3099–3106

Zhang J, Yu J, Zhang Y, Li Q, Gong JR (2011) Visible light photocatalytic H2-production activity of CuS/ZnS porous nanosheets based on photoinduced interfacial charge transfer. Nano Lett 11(11):4774–4779

Zhang Z, Huo H, Wang L, Lou S, Xiang L, Xie B, Wang Q, Du C, Wang J, Yin G (2021) Stacking fault disorder induced by Mn doping in Ni (OH) 2 for supercapacitor electrodes. Chem Eng J 412:128617

Zhu M, Wang C, Meng D, Diao G (2013) In situ synthesis of silver nanostructures on magnetic Fe 3 O 4@ C core–shell nanocomposites and their application in catalytic reduction reactions. J Mater Chem A 1(6):2118–2125